Journal of Nanobiotechnology

RESEARCH Open Access

Spleen-targeted NeoPol-mL242 mRNA vaccine induces robust T-cell responses in a hepatocellular carcinoma model

Yufei Wu[1,2†], Gongrui Sun[1,2†], Wendan Ren[2†], Yang Gui[2], Cong Wang[1], Xinyi Ye[1], Yun Chen[1], Xiufeng Pang[1], Qi Zhang[3*], Zi Jun Wang[2*] and Yuxuan Wu[1,2*]

Abstract

Personalized neoantigen peptide vaccines have shown remarkable anti-tumor activity across diverse cancer types. With the rapid advancement of messenger RNA (mRNA) delivery technologies during the coronavirus disease of 2019 (COVID-19) pandemic, mRNA-based cancer vaccines have emerged as a promising therapeutic approach because of their scalable production, safety, and capacity to elicit potent immune responses. However, the predominant distribution of mRNA delivery systems in the liver may lead to hepatic damage and restrict therapeutic accessibility. In this study, we designed a novel ionizable lipid library to shift the delivery to the spleen. By incorporating an additional anionic lipid, we identified an optimized vaccine formulation, which exhibited efficient uptake by dendritic cells (DCs). Notably, this formulation achieved spleen-selective delivery without requiring targeting ligand modifications, thereby minimizing cytotoxicity risks. Furthermore, the spleen-targeted L242-20Lipo nanoparticle was employed to facilitate the efficient delivery of personalized neoantigen mRNA vaccines. Evaluation in a hepatocellular carcinoma (HCC) model demonstrated that the NeoPol-mL242 mRNA vaccine elicited potent anti-tumor immunity while maintaining an excellent safety profile. These results highlight NeoPol-mL242 as a promising candidate for application in cancer immunotherapy.

Graphical abstract

Schematic illustration of L242-20Lipo for in vivo delivery of personalized neoantigen mRNA. The formulation of spleen-targeted L242-20Lipo and the preparation of personalized neoantigen mRNA vaccines, including B16M01-mL242 for murine melanoma and NeoPol-mL242 for hepatocellular carcinoma, enable precise and effective immune activation.

†Yufei Wu, Gongrui Sun and Wendan Ren contributed equally.

*Correspondence:
Qi Zhang
qi.zhang@zju.edu.cn
Zi Jun Wang
zjwang@yoltx.com
Yuxuan Wu
yxwu@bio.ecnu.edu.cn

Full list of author information is available at the end of the article

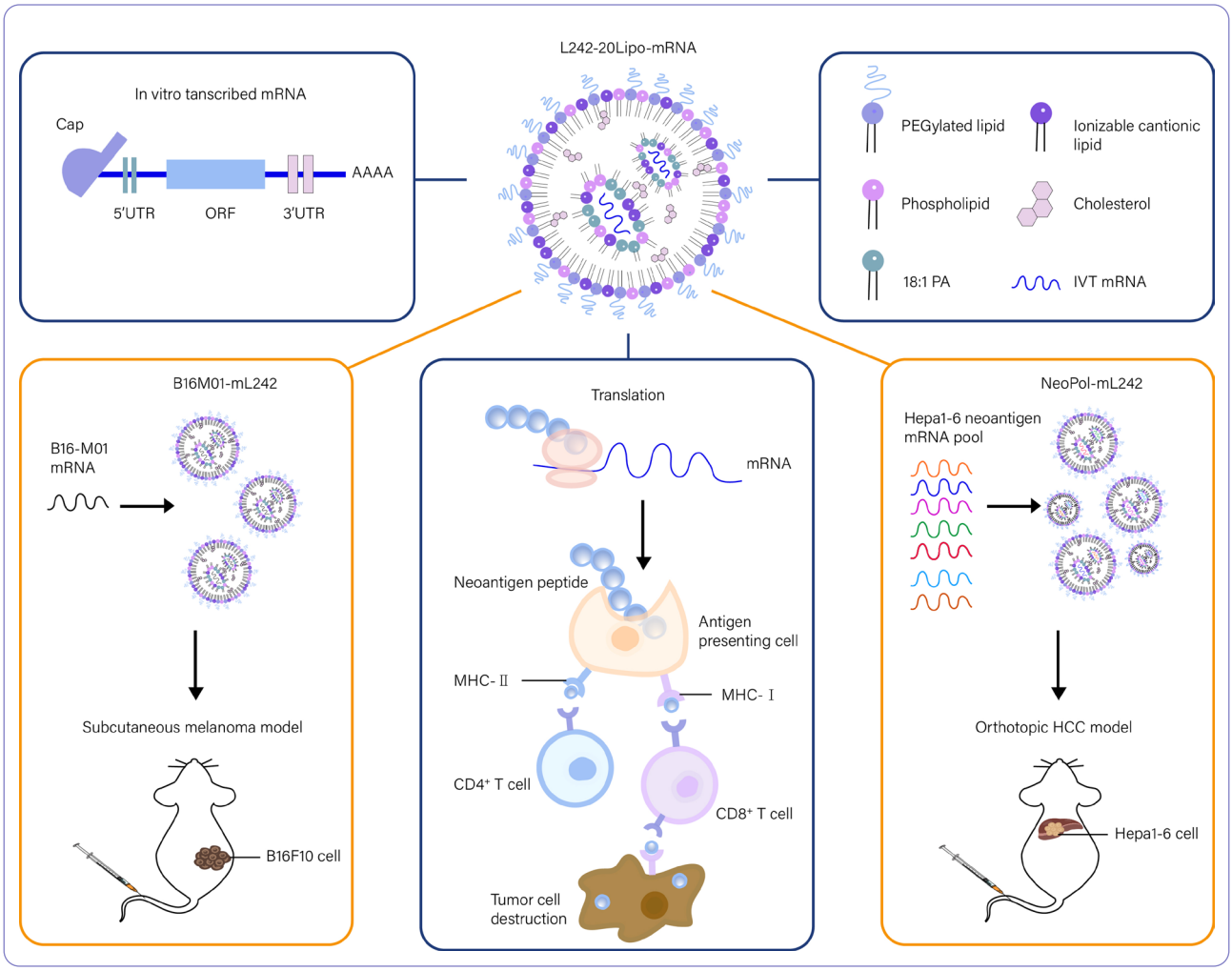

Introduction

Hepatocellular carcinoma (HCC) is the third leading cause of cancer-related deaths worldwide, with a 5-year survival rate below 20% in advanced-stage disease [1, 2]. Surgical resection remains the mainstay treatment for early-stage HCC [3]. Nonetheless, high recurrence rates and limited availability of donor organs for liver transplantation [4] necessitate alternative therapies. Systemic therapies, such as sorafenib [5] and lenvatinib [6], provide modest survival benefits by inhibiting tumor growth and angiogenesis. However, resistance and therapy-related toxicity pose considerable challenges.

Cancer immunotherapy has emerged as an effective anti-tumor strategy that activates the host immune system. Clinically effective modalities consist of immune checkpoint inhibitors [7–9], chimeric antigen receptor T-cell (CAR-T) therapy [10, 11], and bispecific antibodies [12–14]. However, their application in HCC remains constrained primarily due to the immunosuppressive tumor microenvironment, characterized by restricted T-cell infiltration [15]. Considering these drawbacks, strategies that enhance tumor-specific T-cell infiltration and improve immunotherapy outcomes are warranted. The discovery of neoantigens derived from tumor-specific mutations has revolutionized the field of cancer immunotherapy [16, 17]. Compared with tumor-associated antigens (TAAs) and tumor-specific antigens (TSAs) [18–20], personalized neoantigens demonstrate unique advantages in yielding robust tumor-specific T-cell responses while minimizing off-target effects.

Conventional peptide-based neoantigen vaccines encounter clinical challenges, including complex manufacturing processes, structural instability, and restricted capacity in facilitating antigen presentation [21, 22]. In contrast, the mRNA vaccine design process can be promptly initiated upon determination of the target genetic sequence [23]. The exclusive expression of target antigens effectively minimizes off-target immune responses, enhancing the safety and efficacy of the vaccines [24]. Moreover, the inherent characteristics of in vitro transcribed mRNA enable both scalable manufacturing and rapid antigenic adaptation through sequence

modification [25]. However, the initial clinical applications of naked mRNA were limited by inefficient protein translation, enzymatic degradation, and impaired endocytic activity of antigen-presenting cells (APCs) [26].

These limitations necessitated technological advancements. The optimization of mRNA vaccines has focused on two key aspects: the mRNA structure [26] and its delivery systems [27]. mRNA modifications, including changes to the 5' cap [28–30], the 5'-UTR/3'-UTR framework [31, 32], and a 120-nucleotide poly(A) tail [33–35], have enhanced mRNA stability and translational efficiency. On the other hand, effective delivery technology is crucial for therapeutic applications. Among the existing mRNA delivery platforms, including viral vectors [36, 37] and polymeric carriers [38], lipid nanoparticles (LNPs) have emerged as the preferred vehicle. They offer superior mRNA stability, high transfection efficiency, and favorable immunogenicity [39–41].

Tumor neoantigens necessitate processing and presentation through the major histocompatibility complex (MHC) to elicit an immune response. In this context, DCs play a pivotal role in this therapeutic strategy, owing to their ability to capture, process, and present antigens via MHC molecules [42]. Therefore, targeted delivery to lymphoid organs, particularly the spleen, is crucial for ensuring vaccine efficacy [43]. Recent advances in targeted delivery have focused on adjusting the physicochemical properties (e.g., molecular structure, component ratios, and surface chemistry) of LNPs [44]. The surface pH significantly influences their delivery efficiency and in vivo biodistribution [45]. This phenomenon has been demonstrated in selective organ targeting (SORT) studies, which show that negatively charged LNPs preferentially accumulate in the spleen [46].

In this study, we designed a spleen-targeted L242-20Lipo vector for personalized neoantigen mRNA vaccines. This engineering strategy involved comprehensive structural screening of the amino head group, hydrophobic tail, and internal linker of ionizable cationic lipids. Furthermore, through precise optimization of the molar ratio of 18:1 PA, L242-20Lipo nanoparticles demonstrating enhanced splenic tropism were successfully engineered with significantly reduced hepatic distribution. Efficacy validation in hot tumor models has bolstered our confidence in this approach. We engineered NeoPol-mL242 vaccine, which incorporates seven neoantigens from the Hepa1-6 cell line. As expected, NeoPol-mL242 vaccine induced robust anti-tumor immunity in the murine orthotopic HCC model. Taken together, the L242-20Lipo mRNA delivery vector enhanced the delivery effect to the spleen. Importantly, the efficacy and safety of NeoPol-mL242 vaccine highlight its therapeutic potential in cancer immunotherapy.

Results

Design and characterization of an ionizable lipid library

Successful LNP-mediated delivery to the liver and bone marrow was achieved in our previous studies [47, 48]. To enhance immunogenicity via spleen-targeted mRNA delivery, we systematically engineered a library of LNPs by modifying both the head and tail structures with a unique linker (Fig. 1A, Fig. S1A). The ionizable cationic lipids were synthesized by Yoltech Therapeutics (Shanghai, China). Detailed synthetic methods are provided in our patents (WO/2024/152512, WO/2024/193525, and WO/2025/011532). Briefly, twenty-five molecules were synthesized using a standardized three-step process (Fig. 1B). Candidate ionizable lipids were formulated with cholesterol (Chol), 1,2-distearoyl-sn-glycero-3-phosphocholine (DSPC), DMG-PEG2000, and the additional anionic lipid 1,2-dioleoyl-sn-glycero-3-phosphate (18:1 PA). To enhance spleen targeting, we progressively reduced the concentration of 18:1 PA from 30 to 20% and further to 10%, based on previous reports (Table S1) [46]. We evaluated these lipid nanoparticles (LNPs) by delivering GFP mRNA in vivo. The delivery efficiency of the LNPs was directly related to the chemical structure of the ionizable lipid. Notably, LNPs formulated with lipids L221 and L242 demonstrated superior transfection efficiency compared to other candidates (Fig. 1C).

Screening and optimization of LNPs for spleen-targeted mRNA delivery

To identify optimal candidates for splenic delivery, ionizable lipids predicted to exhibit high spleen-targeting efficiency were screened using commercial ACL-0315 as a control. Mice were intravenously injected with 0.5 mg/kg luciferase mRNA (mLuc), followed by fluorescence assessment after 6 h using an in vivo imaging system (Fig. 2A). The bioluminescence distribution in the mice suggested that the optimized molar ratio of the L242 lipid, Chol, DSPC, DMG-PEG, and 18:1 PA was 40:8:30.8:1.2:20 (Fig. 2B, C, Table S1). At this ratio, L242–20Lipo exhibited significantly enhanced splenic accumulation while maintaining minimal hepatic distribution, compared with both L221- and ALC–0315-based formulations (Fig. 2D). Interestingly, the spleen-to-liver signal ratio of L242–20Lipo was >4.5-fold higher than that of L0315–20Lipo, confirming its selective targeting capability (Fig. 2D). To elucidate the association between the physicochemical properties of LNPs and their organ-targeting efficacy, the pKa, particle size, polydispersity index (PDI) and encapsulation efficiency were systematically characterized (Fig. 2E-G, Fig. S2A). Representative cryo-transmission electron microscopy (cryo-TEM) images of L0315-20Lipo, L221-20Lipo and L242-20Lipo revealed no significant differences in apparent size or structure (Fig. 2H). These results indicate that the

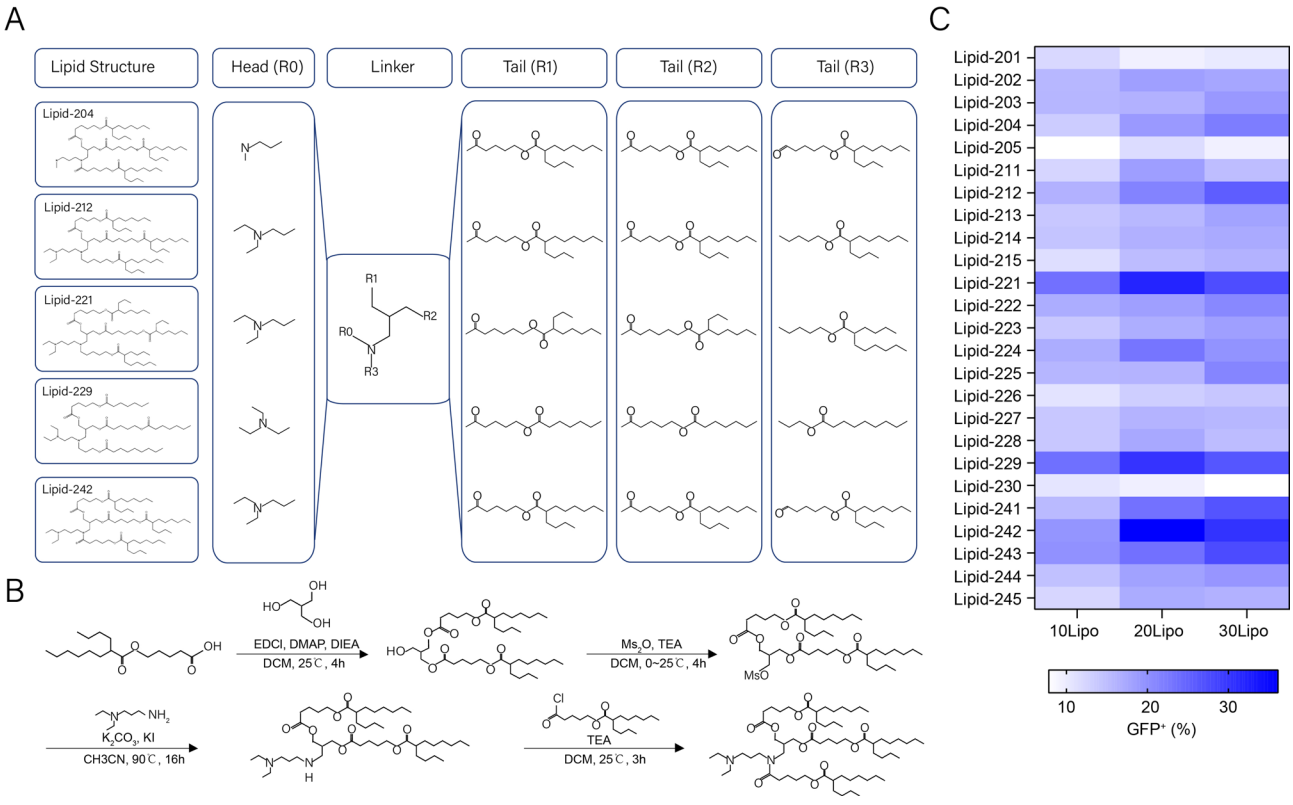

Fig. 1 Candidate ionizable nanoparticles for mRNA delivery. **(A)** The chemical structures of the ionizable liposomes that serve as candidates in this study. (**B**) Representative synthesis pathways and conditions for Lipid-242. (**C**) Heat map image showing in vivo delivering efficiency in splenic cells. C57BL/6 mice were treated with 25 different LNP packages containing GFP mRNA at a dose of 1 mg/kg, and GFP-positive percentage was measured. Data are presented as mean in panel C, $n = 3$

incorporation of 18:1 PA modulated the surface charge characteristics of LNPs, thus improving their spleen-targeting efficacy.

Effect of Spleen-Targeted LNPs on dendritic cells (DCs)

To further investigate the immunotherapeutic potential of spleen-targeted LNPs, we first analyzed their biodistribution among antigen-presenting cells (APCs) and other immune cell populations in Ai14 reporter mice. Candidate LNPs were designed to encapsulate mRNA encoding Cre recombinase (mCre), which mediated excision of LoxP sites to activate tdTomato expression, enabling precise identification of transfected cell subsets (Fig. 3A). Cre mRNA integrity was verified by capillary electrophoresis (CE) (Fig. S3Q). Quantitative analysis reveled Cre-L242-20Lipo uptake in approximately 8% of T cells, 1% of B cells, 27% of dendritic cells (DCs), and 19% of macrophages (Fig. 3B, Fig. S4). Notably, Cre-L242-20Lipo exhibited a 3.4-fold increase in DC transfection compared to Cre-L0315-20Lipo (27% vs. 8%), highlighting its superior targeting ability. These results caught our attention because DCs are crucial for presenting neoantigens to naïve T cells, thereby initiating robust cytotoxic T lymphocyte (CTL) responses. To corroborate these findings, we performed parallel in vivo delivery of GFP mRNA. The DC transfection profile confirmed the targeting advantage of L242-20Lipo with a dose-dependent increase (Fig. 3C). Moreover, our findings demonstrate that mRNA encoding neoantigen (Hepa-M01-mRNA) delivered by L242-20Lipo efficiently active DCs, enhancing CD40 expression by 7.5-fold and CD86 expression by 5.7-fold compared to blank DCs (Fig. 3D, E). All LNPs managed to produce increased expression of CD40 and CD86, which indicates successful BMDC activation. Meanwhile, ELISA analysis confirmed the superior secretion of cytokine IL-12 and TFN-α expression in the supernatant of BMDCs pulsed with neoantigen-LNPs (Fig. 3F, G). Given that the immunostimulatory potency of neoantigen-based cancer therapeutic vaccines is critically contingent upon uptake by APCs, L242-20Lipo emerges as a promising carrier for facilitating antigen delivery and subsequent immune activation.

Validation of B16M01-mL242 in a B16F10 tumor model

Initially, the anti-tumor ability of L242-20Lipo-delivered neoantigen B16M01 mRNA was evaluated in a validated melanoma model (Table S2) [49]. C57BL/6 mice were subcutaneously inoculated with B16F10 cells,

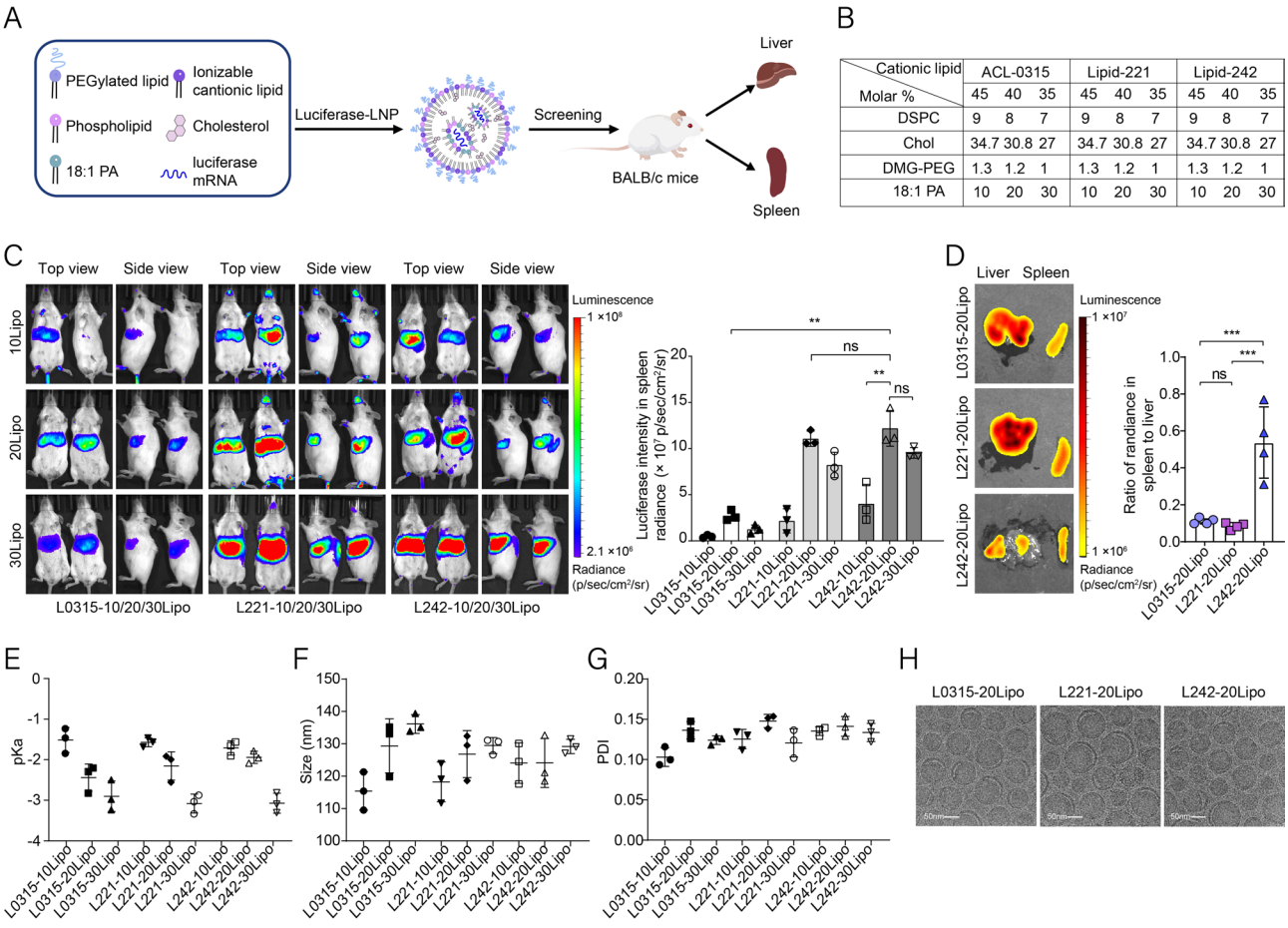

Cationic lipid	ACL-0315			Lipid-221			Lipid-242		
Molar %	45	40	35	45	40	35	45	40	35
DSPC	9	8	7	9	8	7	9	8	7
Chol	34.7	30.8	27	34.7	30.8	27	34.7	30.8	27
DMG-PEG	1.3	1.2	1	1.3	1.2	1	1.3	1.2	1
18:1 PA	10	20	30	10	20	30	10	20	30

Fig. 2 Screening of spleen-targeted lipid nanoparticles. **(A)** The illustration depicts the encapsulation of 0.5 mg/kg luciferase-encoding mRNA in five-component LNPs and the subsequent in vivo screening in mice. (**B**) The chart shows the corresponding composition ratios of ACL-0315, L221 and L242 LNPs containing anionic liposome at molar ratios of 10%, 20% and 30%. (**C**) In vivo imaging graph of mice (left), and the bar chart (right) show the bioluminescence in the spleens of mice. (**D**) Representative images and histogram of bioluminescence distribution in liver and spleen of mice treated with L0315-20Lipo, L221-20Lipo, L242-20Lipo containing luciferase mRNA. (**E-G**) Physicochemical properties of candidate LNPs: (**E**) apparent pKa, (**F**) particle size, and (**G**) polydispersity index. (**H**) Cryo-transmission electron microscopy (Cryo-TEM) images of L0315-20Lipo, L221-20Lipo and L242-20Lipo. Data are plotted as mean ± SD and were analyzed using unpaired two-tailed Student's t-tests in C and D. $^{*}P < 0.05$; $^{**}P < 0.01$; $^{***}P < 0.001$

and then vaccinated with 0.5 mg/kg of B16M01-mL242 on days 4, 11 and 18 (Fig. 4A). Significant immune cell activation was observed in the spleen and lymph nodes of mice treated with B16M01-mRNA/L242-20Lipo (B16M01-mL242) (Fig. 4B, Fig. S5, Fig. S6). Compared with ACL-0315 formulation, which primarily targets the liver, the spleen-targeting L242-20Lipo showed more significant immune activation. B16M01-mL242 vaccination was demonstrated to eradicate tumors and prolong survival, whereas rapid tumor progression was observed in both the wild-type mRNA/L242-20Lipo (B16WT01-mL242) group and the PBS group (Fig. 4C, F). On day 25, the mice vaccinated with B16M01-mL242 showed an approximately 86% reduction in tumor size and weight compared to the PBS group (Fig. 4D, E). $CD4^+$ and $CD8^+$ tumor-infiltrating T cell activation was demonstrated with 3.5% and 6.7% IFN-γ positive cells in the B16M01-mL242 group, compared with 0.4% and 0.5% in the B16WT01-mL242 group (Fig. 4H and Fig. S7). Taken together, L242-20Lipo designed to deliver neoantigen mRNA effectively induces immune activation against melanoma, thereby eradicating the tumor in vivo.

Anti-tumor immunity of NeoPol-mL242 in the orthotopic HCC model

It implies the potential of L242-20Lipo to deliver neoantigen mRNA vaccines across diverse tumor models, as demonstrated by the tumor eradication in the melanoma model. Thus, the immunotherapeutic efficacy of L242-20Lipo-mediated neoantigen mRNA vaccination (NeoPol-mL242) was further investigated in the orthotopic HCC model. NeoPol was composed of neoantigens Hepa-M01 to Hepa-M07, which were identified according to previous research findings (Fig. 5A, Table S2, S3) [50]. As shown in the timeline, mice received three doses of NeoPol-mL242 (Fig. 5B). Tumor progression

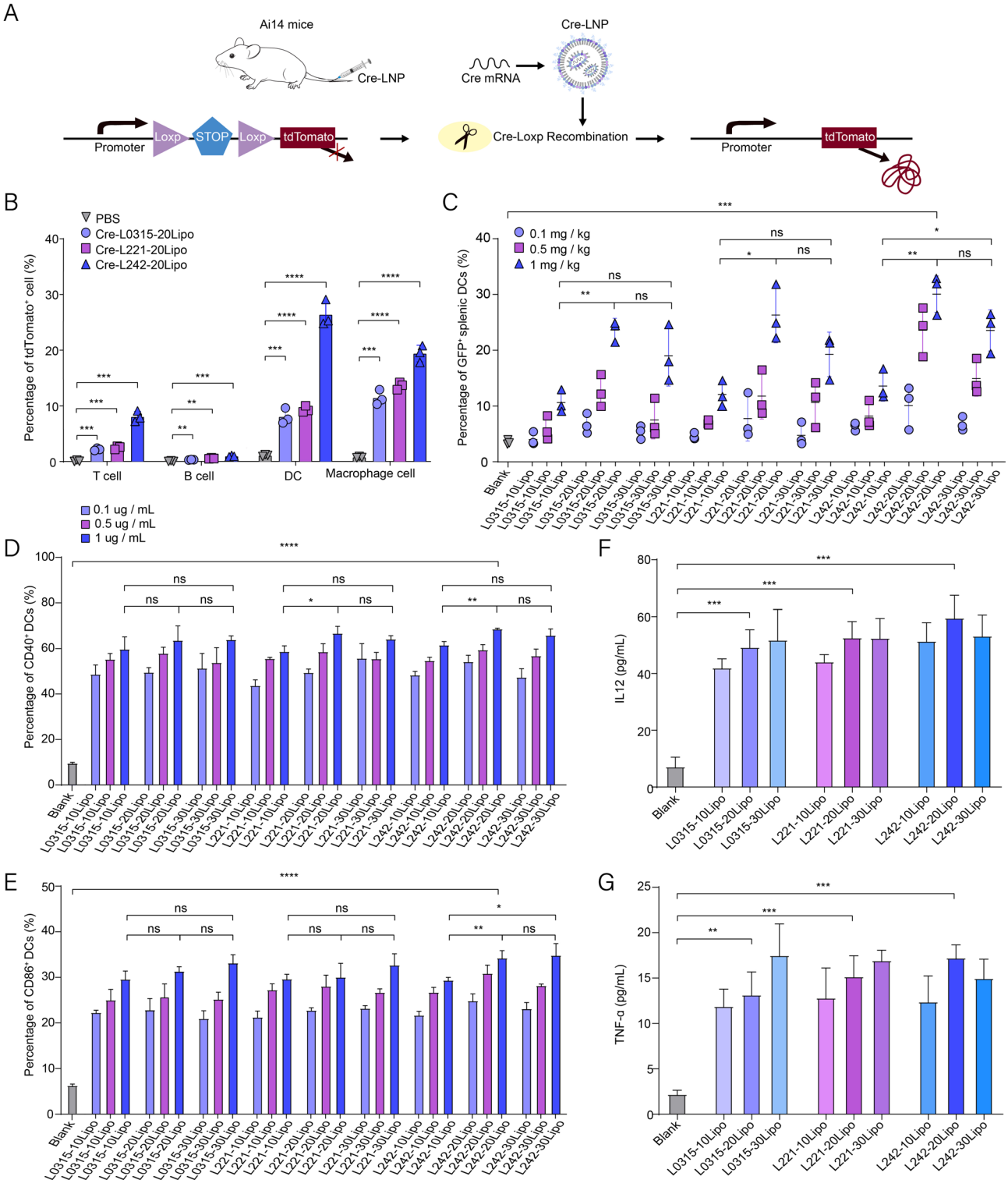

Fig. 3 Exploration of key cells in mRNA presentation. (**A**) Schematic illustration of the mechanism for demonstrating Cre-mRNA distribution in Ai14-tdTomato reporter mice. (**B**) Histogram of the percentage of tdTomato-positive cells in different types of immunocytes 48 h after tail-vein injection of 0.5 mg/kg mCre-L0315-20Lipo, mCre-L221-20Lipo, and mCre-L242-20Lipo. (**C**) Scatter plot of the percentage of GFP-positive dendritic cells (DCs) after treatment with ACL-0315, L221, and L242 LNPs containing different ratios of 18:1 PA at various dosages. (**D**, **E**) Expression of DC activation markers: (**D**) CD40 and (**E**) CD86 positive-percentage of DCs. (**F**, **G**) Cytokine concentration of (**F**) IL-12 and (**G**) TNF-α after treatment with 0.1 ug/mL Hepa-M01-LNPs. Data are presented as means ± SD in B-G ($n = 3$). Independent two-tailed Student's t-tests was used to determine the statistical significance (*$P < 0.05$; **$P < 0.01$; ***$P < 0.001$; ****$P < 0.0001$). Cre mRNA, cyclization recombination mRNA

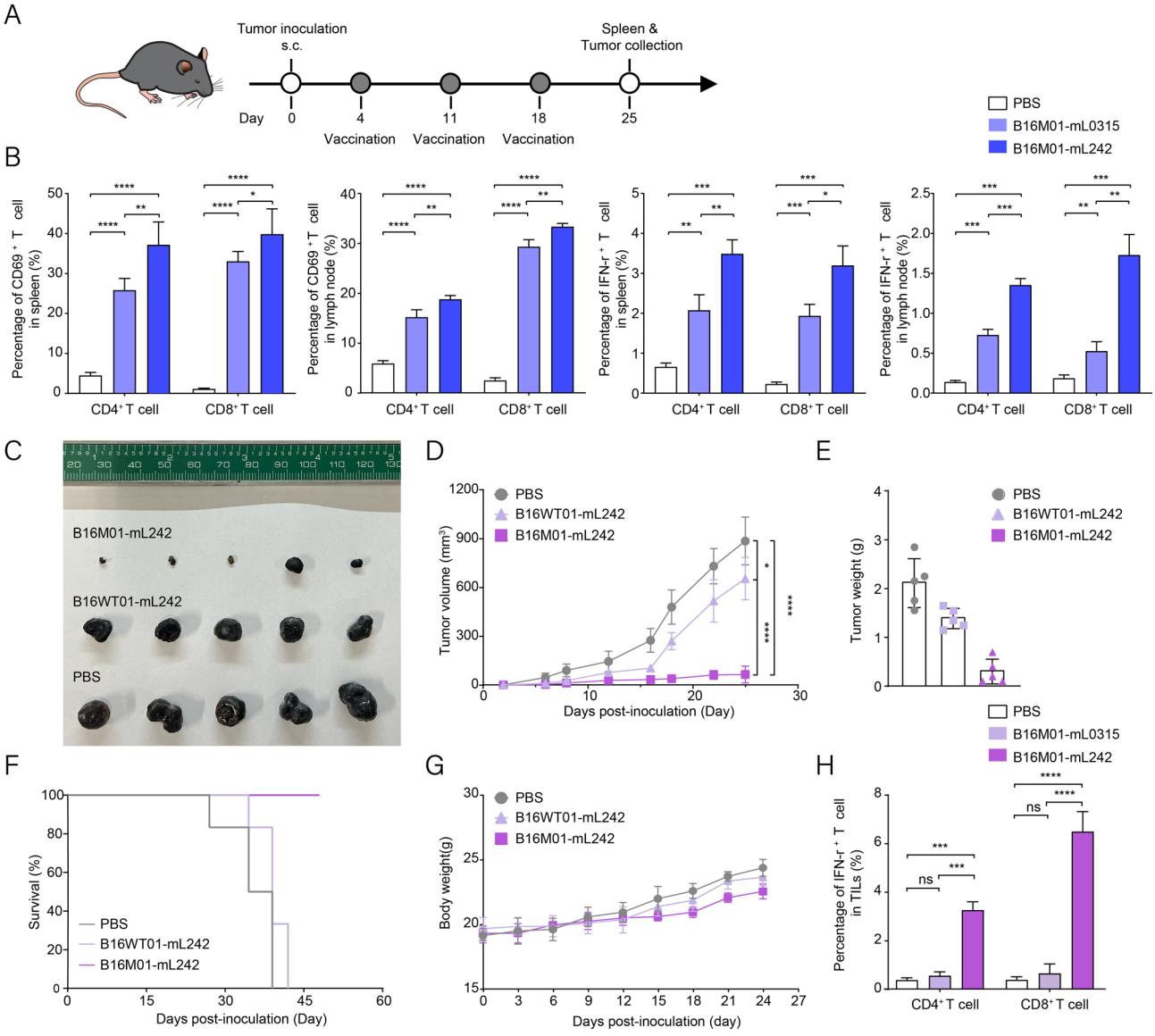

Fig. 4 T-cell responses and anti-tumor efficacy of B16M01-mL242. **(A)** Treatment timeline for vaccination in the subcutaneous B16F10 tumor model ($n = 5$). (**B**) Statistical graphs of the flow cytometry results regarding the percentages of $CD69^+$ T cells and IFN-γ^+ T cells in the spleen and lymph nodes after vaccination. (**C**) Images of isolated tumors of mice treated with B16M01-mL242, B16WT01-mL242, or PBS. (**D**) Tumor growth curves and (**E**) tumor weights for the indicated mouse groups. (**F**) Kaplan–Meier curves for mouse survival in different treatment groups over 48 days. (**G**) Body weight monitoring of mice in each group every 3 days over a 25-day period. (**H**) Representative flow cytometry diagram shows the percentages of IFN-γ^+ T cells within $CD4^+$ and $CD8^+$ TILs. Results are presented as means ± SD. Independent two-tailed Student's t-tests was used to determine the statistical significance ($n = 5$). $^*P < 0.05$; $^{**}P < 0.01$; $^{***}P < 0.001$; $^{****}P < 0.0001$

was monitored throughout the treatment using the in vivo imaging system (Fig. 5C). Compared with the control group, mice vaccinated with NeoPol-mL242 exhibited ~ 90% lower tumor burdens (Fig. 5C, Fig. S8). The 0.5 mg/kg NeoPol-mL242 group showed significant survival extension and weight stability (Fig. 5D, E). Consistently, a higher level of $CD8^+$ T cell infiltration was detected in tumors from NeoPol-mL242-treated mice than in controls (Fig. 5F). Tumor tissues were collected for Ki67 and TUNEL assays to evaluate the tumor-killing ability of NeoPol-mL242 (Fig. 3G). Immunofluorescence results demonstrated a marked decrease in proliferative (Ki67-positive) capacity of tumor cells in mice receiving NeoPol-mL242 vaccination (Fig. 3H). In addition, a significant increase in terminal deoxynucleotidyl transferase-mediated deoxyuridine triphosphate nick end labeling (TUNEL)-positive cells validated the tumor-killing ability of NeoPol-mL242 (Fig. 3I).

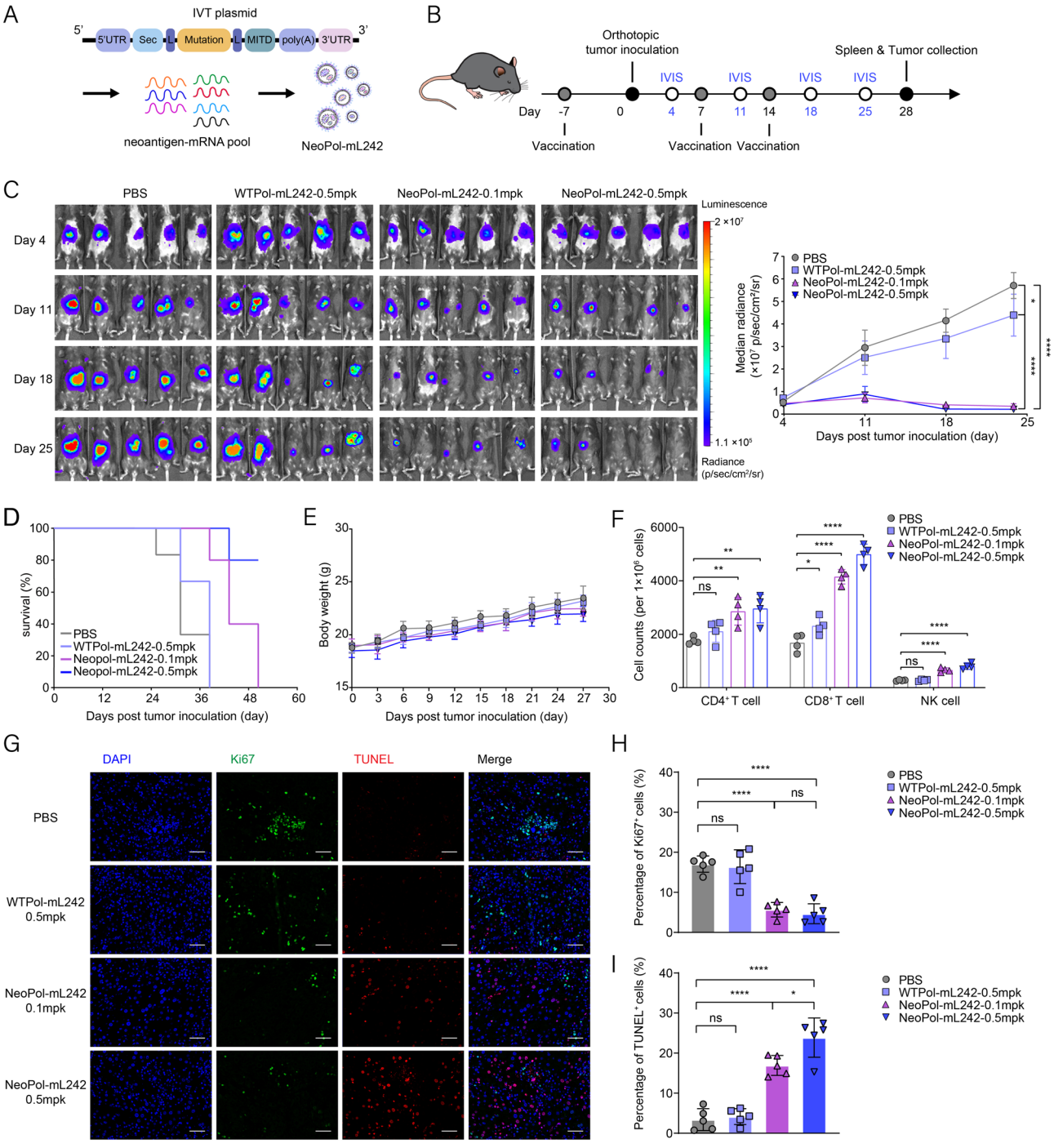

Fig. 5 Tumor cytotoxicity of NeoPol-mL242 in the orthotopic HCC model. (**A**) The schematic illustration shows the workflow for in vitro transcription of neoantigen-encoding mRNA followed by lipid nanoparticle (LNP) formulation. (**B**) Treatment timeline for vaccination in the orthotopic HCC model ($n = 5$). (**C**) Bioluminescence images (left) of C57BL/6 mice treated with NeoPol-mL242 (0.1 mg/kg, 0.5 mg/kg), WTPol-mL242 (0.5 mg/kg), or PBS. Line chart (right) of fluorescence luminescence intensity for tumor burden monitoring every seven days. (**D**) Kaplan–Meier curves for mouse survival over 50 days. (**E**) Body weight monitoring of mice every 3 days. (**F**) Frequency of T and NK cells infiltrating tumors 7 days after the third vaccination. (**G**) Immunofluorescence staining of Ki67 (green) and TUNEL (red) in tumor tissues for proliferation and apoptosis analysis. Staining of DAPI (blue) indicates nucleus. Scale bar, 50 μm. (**H**, **I**) Quantitative analysis of positive cell proportions using ImageJ software: (H) the percentage of Ki67-positive proliferating cells and (**I**) the percentage of TUNEL-positive apoptotic cells. Results are presented as means ± SD for C-F, H and I. Statistical significance was assessed using unpaired Student's t-tests ($n = 4$). *$P < 0.05$; **$P < 0.01$; ***$P < 0.001$, ****$P < 0.0001$. mpk, mg/kg

Immune specificity of NeoPol-mL242 vaccine

Based on the findings aforementioned, we further evaluated neoantigen-specific $CD8^+$ TILs and central memory $CD8^+$ T cells (TCMs, $CD44^+$ and $CD62L^+$) (Fig. 6A-D). Peptide-MHC tetramer staining revealed a higher percentage of intratumoral neoantigen-specific $CD8^+$ T cells in NeoPol-mL242 treated mice (Fig. 6B). Moreover, the percentage of $CD8^+$ TCMs in the mice vaccinated with NeoPol-mL242 was significantly increased (Fig. 6D). These data confirm the neoantigen-specific efficacy of NeoPol-mL242 therapy. To further verified the immune specificity, we assessed the antigen-presenting capacity of mature DCs. BMDCs were stimulated with seven neoantigenic peptides or wild-type peptides and then co-cultured with splenic T cells isolated from mice vaccinated with either NeoPol-mL242 or WTPol-mL242 (Fig. 6D). Ex vivo IFN-γ ELISPOT and flow cytometry assays revealed an obvious activation of T cells via DC-mediated presentation of neoantigens in the NeoPol-mL242 group (Fig. 6F-K). Flow cytometry analysis demonstrated that mice administered 0.5 mg/kg NeoPol-mL242 exhibited statistically significant increases in the frequencies of $CD69^+$ and IFN-γ^+ T cells (Fig. 6F, G). However, DCs pulsed with wild-type peptides failed to activate $CD4^+$ or $CD8^+$ T cells across all experimental groups (Fig. S9). The 0.5 mg/kg dose of NeoPol-mL242 vaccine showed a 3.8-fold increase in spot forming cells over the 0.1 mg/kg dose representing a dose-dependent relationship (Fig. 6H, I). Meanwhile, no significant differences in IFN-γ production were observed between the WTPol-mL242 and PBS groups. Specifically, the proportion of $CD69^+$ activated NK cells in the 0.5 mg/kg NeoPol-mL242 group reached approximately 10.8%, compared to 3.2% in the WTPol-mL242 group (Fig. 6J, K). Experimental results proved that NK cells were markedly activated and cytotoxic (Fig. S10). Taken together, these comprehensive analyses indicate that the NeoPol-mL242 vaccine effectively induces neoantigen-specific T cell immunity via DC-dependent pathways.

Then $CD8^+$ T cells were isolated using fluorescence-activated cell sorting (FACS) and subsequently co-cultured with Hepa1-6 cells to investigate the tumoricidal capacity. Flow cytometry analysis revealed apoptosis in ~42% of Hepa1–6 target cells induced by neoantigenic peptide-stimulated $CD8^+$ T cells from 0.5 mg/kg NeoPol-mL242-treated mice (Fig. 6M). Consistent with fluorescence microscopy imaging, these results indicate the tumor-killing ability of NeoPol-mL242 vaccination (Fig. 6L). Cytokine secretion was also analyzed using enzyme-linked immunosorbent assay (ELISA). Tumor necrosis factor-alpha (TNF-α) level was significantly higher in the 0.5 mg/kg NeoPol-mL242 group, corroborating that NeoPol-mL242 enhances $CD8^+$ T cell-mediated anti-tumor immunity (Fig. 6N). Overall, these results indicated that NeoPol-mL242 could successfully induce a strong neoantigen-specific antitumor response in the murine orthotopic hepatocellular carcinoma model.

Safety assessment of NeoPol-mL242 vaccine in mice

In vivo safety evaluations of the NeoPol-mL242 vaccine were conducted through comprehensive analyses, including serum biochemistry and histopathological examinations (Fig. 7A). Transient elevations in hepatic enzymes, specifically aspartate transaminase (AST) and alanine transaminase (ALT), were observed, peaking at 24 h post-administration (Fig. 7B, C). Nevertheless, these parameters normalized within 72 h in mice treated with NeoPol-mL242. Moreover, no significant differences were detected in alkaline phosphatase (ALP), albumin (ALB), or total protein (TP) levels across treatment groups (Fig. S11). To characterize the inflammatory response, serum concentrations of interleukin-1β (IL-1β), interleukin-6 (IL-6), TNF-α, and interferon-γ-induced protein-10 (IP-10) were quantified using ELISA (Fig. 7D-G). A transient elevation of inflammatory cytokines was observed at 2 h post-vaccination, while all cytokine concentrations returned to baseline within one week. Histopathological assessments of major organs (liver, heart, spleen, lung, and kidney) suggested no pathological alterations in any experimental group (Fig. 7H-J). In addition, no tissue damage was observed across all groups 6 months after injection (Fig. S12). To assess the pharmacokinetics of LNPs, we quantified the amount of GFP mRNA remaining in the plasma after injection of GFP-L242-20Lipo (Fig. 7K). Biodistribution analysis revealed that GFP mRNA expression was predominantly localized in the spleen, with levels declining and nearly undetectable after 96 h (Fig. 7L-N). Together, these data demonstrate the absence of acute toxicity, reinforcing the favorable safety profile of the NeoPol-mL242 vaccine. Furthermore, the low dose vaccine induced robust T cell responses while avoiding significant inflammation or tissue damage, underscoring its clinical application potential.

Discussion

Despite neoantigen-peptide vaccines showing promise in anti-tumor immunotherapy for solid tumors, such as melanoma [51] and pancreatic cancer [52, 53], the role of mRNA-based neoantigen vaccines for HCC models remains largely unexplored. The development of mRNA vaccines for COVID-19 has dramatically advanced technologies in vivo mRNA delivery platforms. Considering that neoantigen immunogenicity necessitates the targeted activation of immune organs, this study focused on spleen-targeted delivery to enhance anti-tumor immunity. In this study, a series of LNP formulations were systematically screened to identify the optimal mRNA

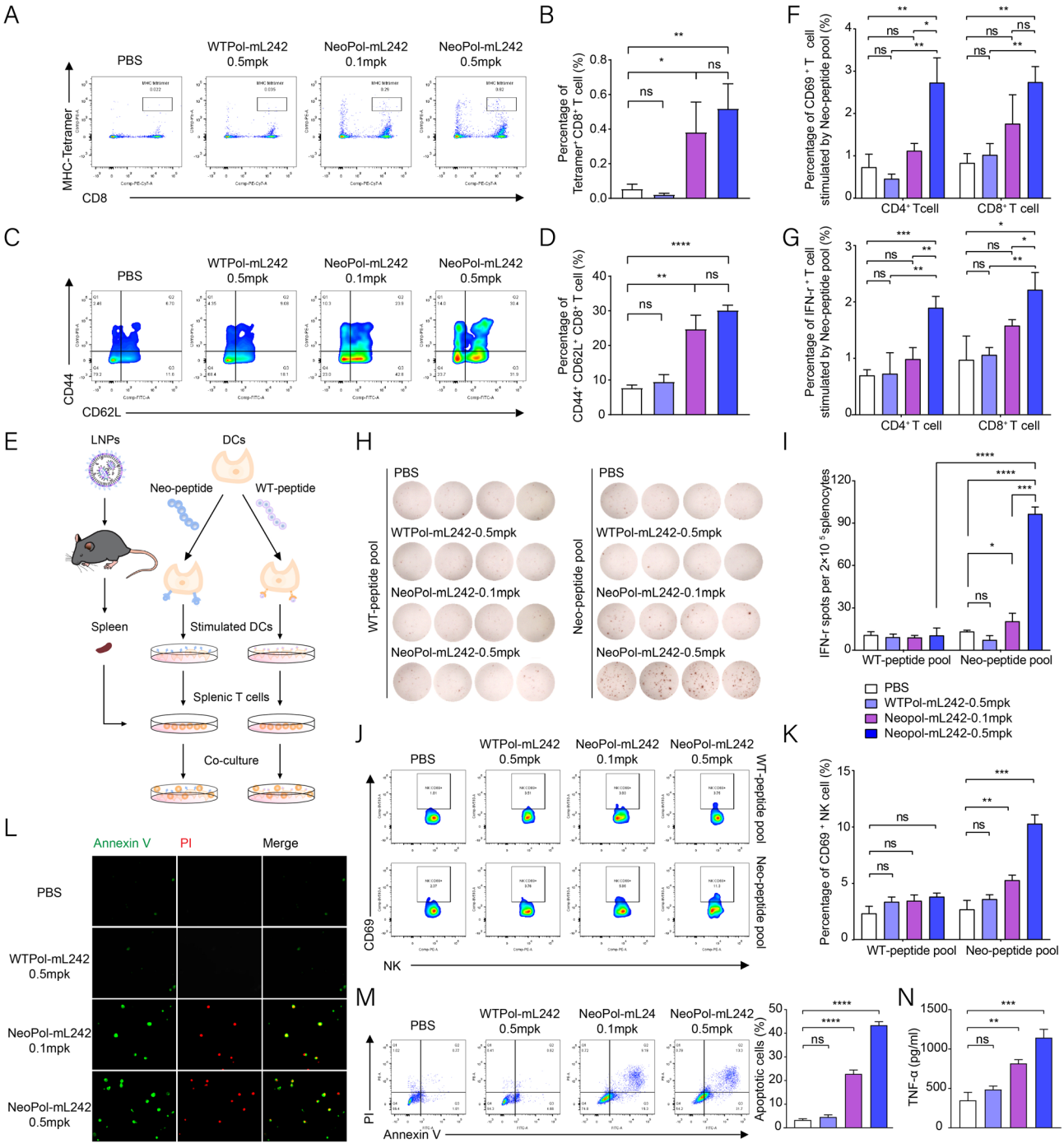

Fig. 6 Immune specificity of NeoPol-mL242 (**A**) Flow cytometry analysis showing the percentage of Ptpn2$_{376–384}$ (RWLYWQPTL): H-2K^{b} specific tumor-infiltrating CD8^{+} T cells. (**B**) Statistical chart of Tetramer^{+} CD8^{+} TILs. (C) Flow cytometry showing the percentage of central memory T cells (T_{CMs}, CD44^{+} and CD62L^{+}) in spleen. (**D**) Statistical chart of T_{CMs}. (**E**) Schematic illustration of co-culturing antigen-stimulated mature bone marrow-derived dendritic cells (BMDCs) with splenic T cells isolated from immunized mice. (**F-G**) Flow cytometry analysis of splenic T cells activated by Mut-peptide pool stimulating DCs. (**F**) Percentage of CD69^{+} CD4^{+} and CD8^{+} T cells 24 h after co-culture. (**G**) Percentage of IFN-γ^{+} CD4^{+} and CD8^{+} T cells 72 h after co-culture. (**H**) ELISpot images of IFN-γ-secreting T cells per 2×10^{5} splenocytes. (**I**) Bar graph of the IFN-γ-positive spot number. (**J**) Representative flow cytometry diagrams of CD69-positive cells within splenic NK cells stimulated by neoantigen pools. (**K**) Statistical chart of CD69^{+} NK cells. (**L**) Fluorescence microscopy images of Hepa1-6 cells after co-culture with stimulated CD8^{+} T cells. Apoptotic cells (green, Annexin V-FITC^{+}), late-stage apoptosis or necrosis (dual-stained green/red, Annexin V-FITC^{+} and propidium iodide^{+}), and viable cells (non-fluorescent) are indicated. (**M**) Flow cytometry analysis of apoptosis (Annexin V/PI staining) in Hepa1-6 cells. (**N**) TNF-α secretion level in culture medium supernatant at 24 h post-stimulation via ELISA. Data are presented as means ± SD ($n=4$). Independent two-tailed Student's t-tests were used. *$P<0.05$; **$P<0.01$; ***$P<0.001$; ****$P<0.0001$. mpk, mg/kg

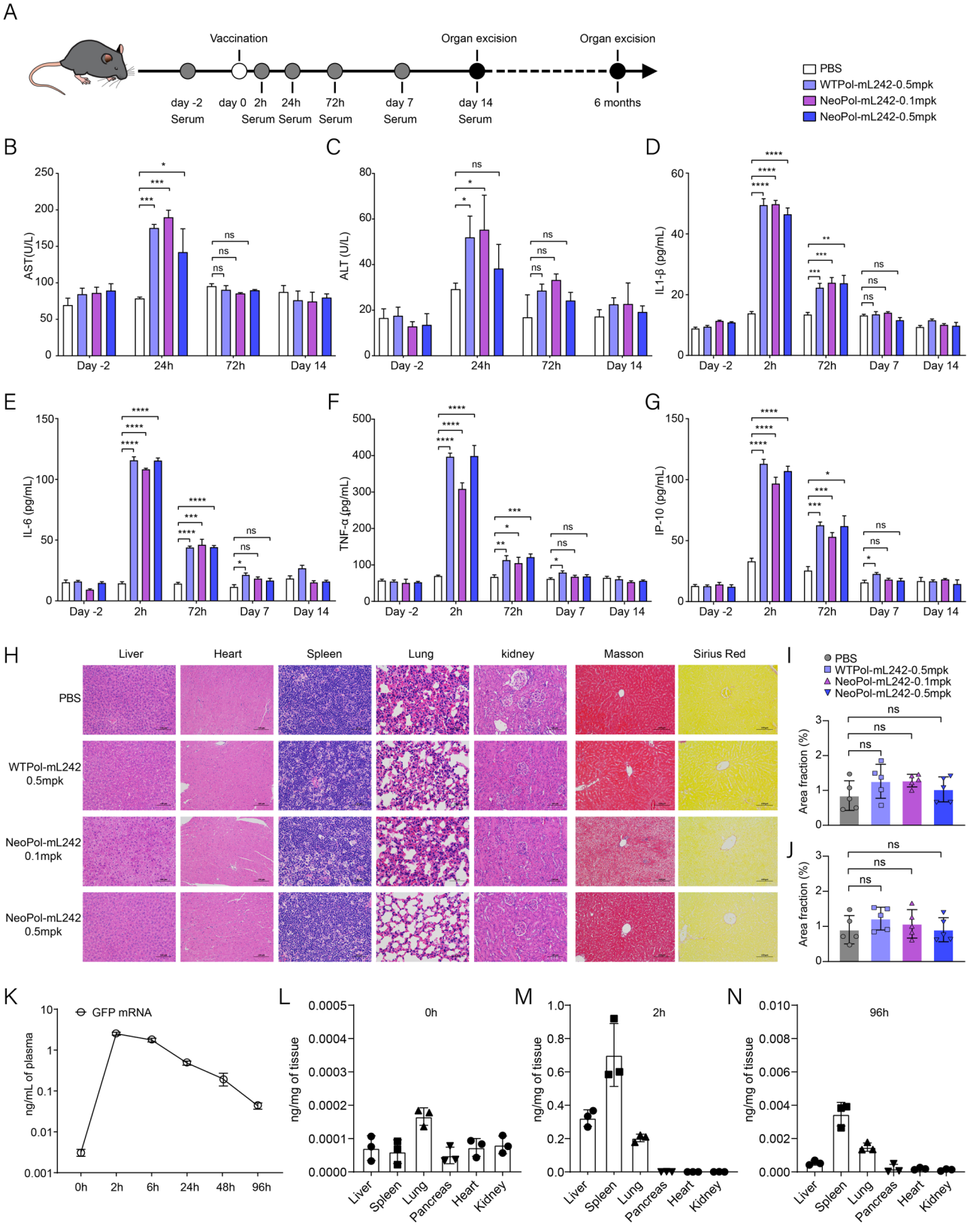

Fig. 7 (See legend on next page.)

(See figure on previous page.)

Fig. 7 Safety assessment of NeoPol-mL242 mRNA vaccine in mice (**A**) Time points for the collection of serum and tissue samples. Serum levels of (**B**) AST and (**C**) ALT in mice at various time points after vaccination with PBS, 0.5 mg/kg WTPol-mL242, 0.1 mg/kg NeoPol-mL242 and 0.5 mg/kg NeoPol-mL242. Serum concentrations of (**D**) IL-1β, (**E**) IL-6, (**F**) TNF-α, and (**G**) IP-10 in mice, measured by ELISA. (**H**) Histopathological analysis showing H&E staining of various tissues, Masson's trichrome staining of liver sections, and Sirius Red staining of liver sections ($n = 5$). (**I**) Percentage of Masson-positive area. (**J**) Percentage of Sirius Red-positive area. (**K**) GFP mRNA level in mouse plasma at various time points up to 96 h after treatment with GFP-L242-20Lipo. (**L-N**) Biodistribution of GFP mRNA in tissues at various time points ($n = 3$). Data are presented as means ± SD in B-G ($n = 4$). Statistical significance was assessed using a two-tailed t test. *$p < 0.05$, **$p < 0.01$, ***$p < 0.001$

delivery vehicles. Among those, L242-20Lipo was identified as the most promising candidate for therapeutic mRNA vaccination.

Initially, the influence of the ionizable lipid structure, particularly the head, linker and tail regions, on splenic mRNA expression was investigated. The optimized cationic lipids were further evaluated with 18:1 PA, an anionic lipid that modulates surface charge. Notably, L242-20Lipo exhibited enhanced spleen-specific delivery of luciferase mRNA (mLuc). Ai14 mice were used to monitor Cre mRNA uptake in splenic immune subsets. The significant increase of fluorescence signals in DCs suggested their presentation of neoantigens, highlighting the clinical potential of L242-20Lipo as a vaccine delivery vector. In addition, serum analysis indicated no persistent abnormalities, indicating minimal hepatotoxic risk of L242-20Lipo. Possibly, the modest hepatic distribution of NeoPol-mL242 may offer therapeutic advantages in HCC by allowing tumor infiltration while maintaining a safety profile.

The B16F10 melanoma model was utilized to validate the therapeutic efficacy of the MHC class II-restricted neoantigen B16-M01 delivered by L242-20Lipo. This formulation mediated complete tumor regression within 25 days, suggesting both the efficacy of the LNP delivery platform and the therapeutic potential of MHC class II-presented neoantigens. This strategy in HCC model, an immunologically resistant malignancy, elicited neoantigen-specific $CD4^+$ and $CD8^+$ T cell responses through coordinated antigen presentation via both MHC classes. NeoPol-mL242 vaccine contains five MHC class I and two class II-restricted neoantigens from Hepa1-6 cells. These findings collectively demonstrate that optimized DC delivery can initiate robust adaptive immunity via both MHC class I and II pathways. Additionally, the platform enables rapid vaccine production within two weeks through simple neoantigen mRNA replacement, showcasing its superior scalability, manufacturability and regulatory feasibility.

The novel spleen-targeting LNP vector, L242-20Lipo, demonstrates superior mRNA delivery to antigen-presenting cells (APCs) compared to ACL-0315 formulations. The efficacy of immune cell-mediated neoantigen recognition primarily depends on effective antigen presentation by APCs. Functional validation confirmed the activation of dendritic cells (DCs) and downstream immune responses, supporting the mechanistic role of APCs in driving vaccine efficacy. Together, these findings position NeoPol-mL242 as a promising platform for presenting personalized neoantigen-mRNA vaccines. However, while preclinical studies in murine melanoma and hepatocellular carcinoma (HCC) models demonstrate proof-of-concept, further investigation is required to evaluate its applicability across broader tumor types and in clinical settings. Strategic combination with checkpoint inhibitors or other immunomodulators may potentiate synergistic therapeutic effects.

Materials and methods

Materials

Ionizable lipid ALC-0315 was purchased from MedChemExpress (Monmouth Junction, NJ, USA). Cholesterol, DSPC and DMG-PEG were obtained from Sigma-Aldrich (St. Louis, MO, USA). 1,2-dioleoyl-sn-glycero-3-phosphate (18:1 PA) was purchased from MilliporeSigma (Burlington, MA, USA). Purified fluorescein isothiocyanate (FITC)-conjugated anti-mouse CD3 antibody (BioLegend, 100203), allophycocyanin (APC)-conjugated anti-mouse CD4 antibody (BioLegend, 116013), peridinin-chlorophyll-protein complex (PerCP)/Cyanine5.5-conjugated anti-mouse CD19 antibody (BioLegend, 152405), phycoerythrin (PE)-conjugated anti-mouse NK1.1 antibody (eBioscience, 12-5941-82), PE/Cyanine7-conjugated anti-mouse CD8 antibody (BioLegend, 100722), APC/Cyanine7-conjugated anti-mouse F4/80 antibody (BioLegend, 157315), APC-conjugated anti-mouse CD11c antibody (BioLegend, 117309), PE-conjugated anti-mouse CD40 antibody (eBioscience, 12-0401-82), PerCP/Cyanine5.5-conjugated anti-mouse CD86 antibody (BioLegend, 159211), FITC-conjugated anti-mouse CD62L antibody (eBioscience, 11-0621-82), PE-conjugated anti-mouse CD44 antibody (eBioscience, 12-0441-82), Brilliant Violet 510-conjugated anti-mouse CD69 antibody (BioLegend, 104531), and Brilliant Violet 421-conjugated anti-mouse IFN-γ antibody (BioLegend, 505829) were obtained from Thermo Fisher Scientific (Waltham, MA, USA). Anti-mouse MHC-Tetramer-PE ($Ptpn2_{376–384}$ (RWLYWQPTL): H-$2K^b$) was obtained from AtaGenix (Wuhan, China).

Cells and animals

Murine B16F10 cells and Hepa1-6 cells were obtained from the Cell Bank of Type Culture Collection (Chinese Academy of Sciences). C57BL/6J mice

(female, 6–8 weeks old) and BALB/c mice (female, 6–8 weeks old) were purchased from the Shanghai Laboratory Animal Center (Shanghai, China). B6; 129S6-Gt(ROSA)26Sor$^{tm14(CAG-tdTomato)Hze}$/J Ai14 mice (female, 6–8 weeks old, 007908) were purchased from The Jackson Laboratory (Bar Harbor, ME, USA). All animal experiments were conducted in strict accordance with the guidelines established by the Shanghai Laboratory Animal Commission. These procedures were approved by the Institutional Animal Care and Use Committee (IACUC) of East China Normal University (approval number: m20240814).

Ionizable lipids synthesis

The ionizable lipid library presented in this study was synthesized following the methodologies described in our patents (WO/2024/152512, WO/2024/193525, and WO/2025/011532), where detailed procedures can be found. The lipids were activated through 2-butyloctanoate esters, followed by amide coupling with a diverse range of diamines. The central pentanedioic acid scaffold was functionalized with N, N-dialkylated diamines of different chain lengths and substitution patterns. Finally, chromatographic purification was performed using silica gel chromatography with a CH_2Cl_2/MeOH gradient. Specifically, 5-(benzyloxy)–5-oxopentyl 2-butyloctanoate (64 g, 163.87 mmol) was hydrogenated using 10% Pd/C (3.49 g) in a MeOH/THF (1:1) solvent mixture. The reaction was conducted at 25 °C for 16 h under hydrogen atmosphere. The product was obtained as a colorless oil (45 g) after filtration and concentration. Subsequently, this intermediate was converted to its corresponding acyl chloride by treatment with oxalyl chloride (2.54 g) and catalytic DMF (49 mg) in DCM at 0 °C for 3 h under nitrogen. After solvent removal, 2 g 5-chloro-5-oxopentyl 2-butyloctanoate was produced. The intermediate (1 g) was coupled with N, N-diethylpropane-1,3-diamine (870 mg) in acetonitrile using K_2CO_3 and KI as catalysts at 90 °C for 16 h. The mixture was then extracted with ethyl acetate (EtOAc) and purified by silica gel chromatography using a DCM/MeOH (50:1 to 10:1). Finally, the product was synthesized by coupling the above intermediate (500 mg) with 5-chloro-5-oxopentyl 2-butyloctanoate (310 mg) in DCM. After silica gel chromatography (40:1 to 15:1), the target compound was isolated as a colorless oil (410 mg).

Formulation of LNPs

To improve delivery efficiency, a series of lipids were synthesized and screened as described previously [46]. Briefly, ionizable lipids, DSPC, cholesterol, and PEG lipid were dissolved in ethanol at different molar ratios. To achieve spleen-targeting, the lipid mixture was combined with anionic lipid 18:1 PA. Notably, the ionizable cationic lipids were procured from YolTech Therapeutics (Shanghai, China). The lipid-mRNA combination was prepared using a microfluidic mixer (Precision Nanosystems, Vancouver, BC), at an aqueous-ethanol flow rate ratio of 3:1 to achieve the desired lipid-to-mRNA weight ratio of 40:1. Subsequently, the LNPs were diluted in PBS to a concentration of 0.5 ng/μl mRNA for in vitro assays. This preparation was further concentrated using Amicon Ultra-15 mL Centrifugal Filter Units (Millipore Sigma), sterilized by filtration through 0.22-μm filters, and stored at −80 °C for future use. Detailed formulation information is described in Table S1. The physicochemical properties of the LNPs, such as particle size, polydispersity index and zeta potential were systematically characterized by dynamic light scattering using the NANO ZS3600 (Malvern, Worcestershire, UK). Additionally, RNA encapsulation efficiency within the LNPs was determined with the Quant-iT Ribogreen Assay (Life Technologies, R11490).

Identification of personalized neoantigens

Candidate neoantigens were primarily derived from non-synonymous mutations. HCC neoantigens were identified through genomic and transcriptomic sequencing of liver tissue from wild-type C57BL/6 mice and the Hepa1-6 cell line (variant allele frequency ≥ 10%, sequencing depth ≥ 20). The immunogenicity of each candidate was further predicted using the NetMHCpan binding affinity predictor (IC50 < 500 nM to H-2K^b), as described by Chen et al. [50]. In this study, one B16-M01 [49] and seven Hepa1-6 neoantigens (9-mer mutant) [50] were selected to prepare mRNA vaccinations (Table S2).

Design and synthesis of neoantigen mRNAs

mRNAs encoding luciferase, GFP, Cre recombinase and neoantigens were synthesized using the HiScribe T7 High Yield RNA Synthesis Kit (NEB, E2040S). The linearized DNA template encompassed 5' and 3' untranslated regions as well as a polyadenylated [poly(A)] tail. To enhance both stability and translational efficiency, the mRNA was capped using TriLink CleanCap Reagent AG (TriLink, N-7113), adhering to the manufacturer's protocol. Meanwhile, uridine triphosphate (UTP) was substituted with 1-methylpseudoUTP during transcription. Subsequently, the synthesized mRNAs were purified with the RNeasy Mini Kit (QIAGEN, 74143), following the manufacturer's protocol. RNA concentration was determined using a NanoDrop spectrophotometric measurement at 260 nm, and RNA quality was evaluated by analyzing transcript integrity and size distribution using an Agilent Bioanalyzer 2100 system.

In vivo screening of mLuc LNPs

To systematically assess the performance of different LNP formulations (as outlined in Table S1), BALB/c mice received luciferase-encoding mRNA at a dose of 0.5 mg/kg through an intravenous tail vein injection. 6 h after the injection, they received D-luciferin (BD Bioscience) intraperitoneally at a dose of 25 mg/kg based on body weight. After fifteen-minute incubation, bioluminescence was captured using the In Vivo Imaging System (PerkinElmer, Waltham, MA). To further evaluate tissue-specific transfection efficiency, the liver and spleen were surgically excised and subjected to imaging analysis.

Spleen-targeted delivery of Cre mRNA in Ai14 mice

Ai14 mice received intravenous injections of Cre mRNA at a dose of 0.5 mg/kg to determine their effect on immune subsets. 72 h post-injection, mice were imaged using the In Vivo Imaging System (PerkinElmer, Waltham, MA). Subsequently, reporter protein expression was assessed via flow cytometry. Spleen cell suspensions were prepared by disruption and filtration through a 40-μm strainer. 1×10^6 cells were incubated with 100 μL of flow cytometry staining buffer (eBioscience) containing a panel of fluorescent antibodies: FITC anti-CD3, PerCP-Cy5.5 anti-CD19, APC-Cy7 anti-F4/80 and APC anti-CD11c. After 1 h of incubation at 4 °C, cells were analyzed by flow cytometer (Fortessa, BD Biosciences). Data processing was conducted using FlowJo-v10, with gating strategies provided in Fig. S3A.

BMDC activation assay

Bone marrow-derived dendritic cells (BMDCs) were isolated from the femurs of C57BL/6 mice, and cultured in the presence of 10 ng/mL IL-4 (R&D Systems, 404-ML-010/CF) and 20 ng/mL mGM-CSF (R&D Systems, 415-ML-020/CF) to promote differentiation. Then, the cells were treated with Hepa-M01-mRNA-loaded LNPs for 24 h. To evaluate DC activation, expression of CD40 and CD86 was analyzed by flow cytometry, while the secretion of IL-12 and TNF-α was quantified using enzyme-linked immunosorbent assay (ELISA).

Subcutaneous B16F10 melanoma model

C57BL/6 mice were subcutaneously injected with 5×10^5 B16F10 cells and randomly assigned to three groups: B16M01-mL242, B16WT01-mL242, and PBS control (0.5 mg/kg; $n = 5$ per group). Tumor volume was measured every 3–6 days after transplantation with calipers and calculated according to the formula: $(A \times B^2)/2$ (where A and B denote the largest and smallest tumor diameter, respectively). On day 25 post-inoculation, tumors were harvested, photographed and weighed. B16F10 cells were maintained in complete Dulbecco's Modified Eagle's Medium (DMEM) at 37 °C with 5% CO_2.

Orthotopic Hepa1-6 HCC model

To investigate the efficacy of neoantigen mRNA treatment, an orthotopic HCC model was developed utilizing female C57BL/6 mice (aged 6–8 weeks; $n = 5$). On day 0, a mixture of 3×10^5 Hepa1-6-luciferase cells and Matrigel was injected into the liver subcapsular space. Subsequently, on days 7 and 14, treatment groups received intravenous tail vein injections of neoantigen mRNAs formulated with L242-20Lipo at doses of either 0.1 mg/kg or 0.5 mg/kg in a total volume of 200 μL. In contrast, control groups received either 0.5 mg/kg wild-type antigen mRNA or PBS. Tumor burden was monitored weekly using an IVIS Spectrum animal imaging system (PerkinElmer, Waltham, MA). Photon emission was quantified 15 min after D-luciferin injection, and then in vivo bioluminescence within regions of interest was calculated using IVIS Living Image 4.0 software. On day 28, tumor tissues were collected for immunofluorescence analysis, and splenic lymphocytes were isolated for immunostimulation detection.

Immunofluorescence analysis

Tumor tissues were fixed in 4% neutral-buffered paraformaldehyde (PFA) at 4 °C for 24 h. Then, the tissues were cryoprotected in 30% sucrose solution at 4 °C for 12 h. The samples were embedded in Optimal Cutting Temperature (OCT) compound (Tissue Tek, 4583), frozen at − 80 °C for 12 h, and sectioned into 10-μm slices using a cryostat microtome (Thermo Scientific). For TUNEL assay, the 10-μm slices were incubated with Alexa Fluor 546-labeled deoxyuridine triphosphate for 1 h. For immunofluorescence staining, tissue sections were subjected to antigen retrieval by heat treatment, blocked, and incubated with FITC-conjugated anti-Ki67 antibody. After washing, the slides were mounted with antifade medium containing DAPI and imaged using an Olympus BX53 upright fluorescence microscope. Statistics were performed using ImageJ software.

Flow cytometry analysis

For flow cytometry analysis, single-cell suspensions were prepared from tumors, spleens and lymph nodes. Cells were incubated with fluorochrome-conjugated antibodies in 0.5% bovine serum albumin for 30 min in the dark. Next, intracellular staining was conducted following an established protocol [54]. Briefly, cells were fixed with 0.05% glutaraldehyde (Sigma, 111-30-8) at room temperature for 10 min, followed by permeabilization with 0.1% Triton X-100 (Thermo Fisher Scientific, HFH10) for an additional 15 min. They were stained with anti-mouse IFN-γ-BV421 mAb (BioLegend, 505829) for 30 min at 4 °C in the dark. Finally, flow cytometry analysis was conducted using a flow cytometer (Fortessa, BD, USA), and the acquired data were analyzed with FlowJo v.10 to

comprehensively assess cell subsets. The gating strategies are illustrated in Fig. S4.

ELISPOT assay

For BMDC stimulation, 5×10^4 cells were pulsed with 2 μg/mL of each neoantigen peptide. Subsequently, these BMDCs were co-incubated with 5×10^5 splenic T cells in 96-well Multiscreen plates pre-coated with anti-IFN-γ antibody (Abcam, ab64029). The co-culture was maintained at 37 °C with 5% CO_2 for 48 h. IFN-γ spot-forming cells were visualized using the ELISPOT Analysis System (SinSage, AT-Spot-2200). Finally, images were captured and the spot number for each group was calculated automatically, facilitating the precise quantification of immune responses.

In vitro cytotoxicity assay of T cells

To assess the cytotoxic activity of splenic $CD8^+$ T cells, cells were labeled with anti-mouse CD3-FITC, anti-mouse CD4-APC, and anti-mouse CD8-PE/Cyanine7 antibodies. Then, $CD3^+CD4^-$ $CD8^+$ T cells were sorted by FACS on a BD FACSAria III (BD Biosciences, USA). For the cytotoxicity assay, $CD8^+$ T cells were co-cultured with Hepa1-6 cells, and apoptosis induction was evaluated by dual staining with Annexin V-FITC (Invitrogen, A10788) and propidium iodide (PI; Invitrogen, A10788). Flow cytometric analysis was conducted on a BD Fortessa (BD Biosciences, USA). Additionally, Hepa1-6 cell apoptosis was confirmed by fluorescence microscopy.

Histopathological analysis

For histological evaluation, tissues from murine liver, heart, spleen, lungs, and kidneys were collected and fixed in 4% paraformaldehyde at 25 °C for 12 h. Fixed tissues were dehydrated through a graded ethanol-xylene gradient, and then embedded in paraffin. Then, 4-μm sections were prepared using a rotary microtome (Leica, RM2235) and stained with hematoxylin and eosin (H&E), Masson, and Sirius Red [55]. Finally, slides were examined under an upright fluorescence microscope (Olympus, BX53) to assess histopathological alterations.

Serum biochemistry

C57BL/6 mice ($n = 4$ per group) were administered intravenously NeoPol-mL242 (0.1 mg/kg or 0.5 mg/kg), WTPol-mL242 (0.5 mg/kg), or PBS (control). Blood samples were collected 2 h, 24 h, 72 h, 7 days, and 14 days post-injection. They were allowed to clot at room temperature for 1 h, and then centrifuged at 1,000 × g for 10 min to isolate the serum. Serum levels of aspartate aminotransferase (AST), alanine aminotransferase (ALT), alkaline phosphatase (ALP), albumin (ALB), and total protein (TP) were quantified using the Aspartate Aminotransferase Assay Kit, Alanine Aminotransaminase Assay Kit, Alkaline Phosphatase Assay Kit, Albumin Assay Kit, and Total Protein Assay Kit (Sailuofei Biotechnology, China), respectively, following the manufacturer's protocols. To evaluate systemic inflammatory responses, serum concentrations of interleukin-6 (IL-6), tumor necrosis factor-α (TNF-α), interferon gamma-induced protein 10 (IP-10), and interleukin-1β (IL-1β) were measured using the Mouse IL-6 ELISA Kit (BioLegend, 431307), Mouse TNF-α ELISA Kit (Abcam, ab208348), Mouse IP-10 ELISA Kit (Abcam, ab260067), and Mouse IL-1β Pre-coated ELISA Kit (Dakewe, 1210122), respectively.

RT-qPCR

Organ tissues (liver, spleen, lungs, pancreas, heart and kidneys) were homogenized using a homogenizer (TissueMaster). Total RNA was isolated using TRIzol extraction Reagent (TS424, Sigma) following the manufacturer's protocol. RNA integrity was verified by Nanodrop prior to reverse transcription. cDNA synthesis was performed using PrimeScript RT-PCR (RR036A, TaKaRa). Quantitative real-time PCR (RT-qPCR) was conducted with SYBR Green SuperMix (11202ES08, Yeasen, Shanghai, China). All mRNA expression levels were normalized to the housekeeping gene glyceraldehyde-3-phosphate dehydrogenase (GAPDH). Primer sequences used for RT-qPCR are listed in Table S4.

Data analysis

Data were analyzed using unpaired two-tailed Student's t-tests in GraphPad Prism V.9.0 (GraphPad, San Diego, CA). Numerical variables are reported as mean ± standard deviation (SD). Statistical significance was set as * $p < 0.05$, ** $p < 0.01$, *** $p < 0.001$, and **** $p < 0.0001$. To ensure robust evaluation, at least three biologically independent experiments were conducted for all animal studies and cell-based experiments.

Supplementary Information

The online version contains supplementary material available at https://doi.org/10.1186/s12951-025-03681-8.

Supplementary Material 1

Acknowledgements

We are grateful to the Instruments Sharing Platform of the School of Life Sciences, East China Normal University. We thank YolTech Therapeutics for supplying mRNA and LNP reagents, as well as technical assistance in LNP formulation.

Author contributions

Y.W. : Writing – original draft, Project administration, Methodology, Visualization, Data curation. G.S. : Writing – original draft, Project administration, Methodology, Data curation. W.R. : Methodology, Resources. Y.G. : Methodology, Resources. C.W. : Project administration. X.Y. : Project administration. Y.C. : Project administration. X.P. : Supervision, Resources. Q.Z. : Supervision, Resources. Z.W. : Supervision, Resources, Conceptualization. Y.W. : Writing – review & editing, Writing – original draft, Visualization, Funding acquisition, Supervision, Conceptualization.

Data availability
No datasets were generated or analysed during the current study.

Declarations

Competing interests
The authors declare no competing interests.

Author details
[1]Shanghai Key Laboratory of Regulatory Biology, Institute of Biomedical Sciences, School of Life Sciences, East China Normal University, Shanghai 200241, China
[2]YolTech Therapeutics, Shanghai 201109, China
[3]Department of Hepatobiliary and Pancreatic Surgery, The First Affiliated Hospital, Zhejiang University School of Medicine, Hangzhou 310003, China

Received: 14 June 2025 / Accepted: 18 August 2025
Published online: 02 September 2025

References

1. Siegel RL, Miller KD, Fuchs HE, Jemal A. Cancer statistics, 2021. CA Cancer J Clin. 2021;71(1):7–33.
2. Yang JD, Hainaut P, Gores GJ, Amadou A, Plymoth A, Roberts LR. A global view of hepatocellular carcinoma: trends, risk, prevention and management. Nat Rev Gastroenterol Hepatol. 2019;16(10):589–604.
3. Chen J, Chen J, Xu Q. Current developments and challenges of mRNA vaccines. Annu Rev Biomed Eng. 2022;24(1):85–109.
4. Hester CA, Yopp AC. Surgical Therapies in Hepatocellular Carcinoma, Hepatocellular Carcinoma2019, pp. 145–167.
5. Wilhelm S, Carter C, Lynch M, Lowinger T, Dumas J, Smith RA, Schwartz B, Simantov R, Kelley S. Discovery and development of sorafenib: a multikinase inhibitor for treating cancer. Nat Rev Drug Discov. 2006;5(10):835–44.
6. Wang S, Wang Y, Yu J, Wu H, Zhou Y. Lenvatinib as first-line treatment for unresectable hepatocellular carcinoma: a systematic review and meta-analysis. Cancers (Basel). 2022. https://doi.org/10.3390/cancers14225525.
7. Robert C. A decade of immune-checkpoint inhibitors in cancer therapy. Nat Commun. 2020. https://doi.org/10.1038/s41467-020-17670-y.
8. Alturki NA. Review of the immune checkpoint inhibitors in the context of cancer treatment. J Clin Med. 2023. https://doi.org/10.3390/jcm12134301.
9. Meng L, Wu H, Wu J, Ding Pa, He J, Sang M, Liu L. Mechanisms of immune checkpoint inhibitors: insights into the regulation of circular RNAs involved in cancer hallmarks. Cell Death Dis. 2024. https://doi.org/10.1038/s41419-023-06389-5.
10. Khan SH, Choi Y, Veena M, Lee JK, Shin DS. Advances in CAR T cell therapy: antigen selection, modifications, and current trials for solid tumors. Front Immunol. 2025. https://doi.org/10.3389/fimmu.2024.1489827.
11. Sterner RC, Sterner RM. CAR-T cell therapy: current limitations and potential strategies. Blood Cancer J. 2021. https://doi.org/10.1038/s41408-021-00459-7.
12. Klein C, Brinkmann U, Reichert JM, Kontermann RE. The present and future of bispecific antibodies for cancer therapy. Nat Rev Drug Discov. 2024;23(4):301–19.
13. Labrijn AF, Janmaat ML, Reichert JM, Parren PWHI. Bispecific antibodies: a mechanistic review of the pipeline. Nat Rev Drug Discov. 2019;18(8):585–608.
14. Stadler CR, Bähr-Mahmud H, Celik L, Hebich B, Roth AS, Roth RP, Karikó K, Türeci Ö, Sahin U. Elimination of large tumors in mice by mRNA-encoded bispecific antibodies. Nat Med. 2017;23(7):815–7.
15. Yang C, Zhang H, Zhang L, Zhu AX, Bernards R, Qin W, Wang C. Evolving therapeutic landscape of advanced hepatocellular carcinoma. Nat Reviews Gastroenterol Hepatol. 2022;20(4):203–22.
16. Hu Z, Leet DE, Allesøe RL, Oliveira G, Li S, Luoma AM, Liu J, Forman J, Huang T, Iorgulescu JB, Holden R, Sarkizova S, Gohil SH, Redd RA, Sun J, Elagina L, Giobbie-Hurder A, Zhang W, Peter L, Ciantra Z, Rodig S, Olive O, Shetty K, Pyrdol J, Uduman M, Lee PC, Bachireddy P, Buchbinder EI, Yoon CH, Neuberg D, Pentelute BL, Hacohen N, Livak KJ, Shukla SA, Olsen LR, Barouch DH, Wucherpfennig KW, Fritsch EF, Keskin DB, Wu CJ, Ott PA. Personal neoantigen vaccines induce persistent memory T cell responses and epitope spreading in patients with melanoma. Nat Med. 2021;27(3):515–25.
17. Ott PA, Hu Z, Keskin DB, Shukla SA, Sun J, Bozym DJ, Zhang W, Luoma A, Giobbie-Hurder A, Peter L, Chen C, Olive O, Carter TA, Li S, Lieb DJ, Eisenhaure T, Gjini E, Stevens J, Lane WJ, Javeri I, Nellaiappan K, Salazar AM, Daley H, Seaman M, Buchbinder EI, Yoon CH, Harden M, Lennon N, Gabriel S, Rodig SJ, Barouch DH, Aster JC, Getz G, Wucherpfennig K, Neuberg D, Ritz J, Lander ES, Fritsch EF, Hacohen N, C.J., Wu. An immunogenic personal neoantigen vaccine for patients with melanoma, Nature 547(7662) (2017) 217–221.
18. Hollingsworth RE, Jansen K. Turning the corner on therapeutic cancer vaccines. NPJ Vaccines. 2019. https://doi.org/10.1038/s41541-019-0103-y.
19. Li J, Xiao Z, Wang D, Jia L, Nie S, Zeng X, Hu W. The screening, identification, design and clinical application of tumor-specific neoantigens for TCR-T cells. Mol Cancer. 2023. https://doi.org/10.1186/s12943-023-01844-5.
20. Vincent CMLaK. Noncoding regions are the main source of targetable tumor-specific antigens. Sci Transl Med (2018).
21. Chen X, Yang J, Wang L, Liu B. Personalized neoantigen vaccination with synthetic long peptides: recent advances and future perspectives. Theranostics. 2020;10(13):6011–23.
22. Melief CJM, van der Burg SH. Immunotherapy of established (pre)malignant disease by synthetic long peptide vaccines. Nat Rev Cancer. 2008;8(5):351–60.
23. Wang Y, Zhang Z, Luo J, Han X, Wei Y, Wei X. mRNA vaccine: a potential therapeutic strategy. Mol Cancer. 2021. https://doi.org/10.1186/s12943-021-01311-z.
24. Kang DD, Li H, Dong Y. Advancements of in vitro transcribed mRNA (IVT mRNA) to enable translation into the clinics. Adv Drug Deliv Rev. 2023. https://doi.org/10.1016/j.addr.2023.114961.
25. Chaudhary N, Weissman D, Whitehead KA. mRNA vaccines for infectious diseases: principles, delivery and clinical translation. Nat Rev Drug Discovery. 2021;20(11):817–38.
26. Ma Y, VanKeulen-Miller R, Fenton OS. mRNA lipid nanoparticle formulation, characterization and evaluation. Nat Protoc (2025).
27. Liu C, Shi Q, Huang X, Koo S, Kong N, Tao W. mRNA-based cancer therapeutics. Nat Rev Cancer. 2023;23(8):526–43.
28. Kore AR. Locked nucleic acid (LNA)-modified dinucleotide mRNA cap analogue: synthesis, enzymatic incorporation, and utilization. J Am Chem Soc. 2009;131:6364–5.
29. Julius C, Yuzenkova Y. Noncanonical RNA-capping: discovery, mechanism, and physiological role debate. WIREs RNA. 2018. https://doi.org/10.1002/wrna.1512.
30. Kowalska J, Wypijewska del Nogal A, Darzynkiewicz ZM, Buck J, Nicola C, Kuhn AN, Lukaszewicz M, Zuberek J, Strenkowska M, Ziemniak M, Maciejczyk M, Bojarska E, Rhoads RE, Darzynkiewicz E, Sahin U, Jemielity J. Synthesis, properties, and biological activity of boranophosphate analogs of the mRNA cap: versatile tools for manipulation of therapeutically relevant cap-dependent processes. Nucleic Acids Res. 2014;42(16):10245–64.
31. Mayr C. What are 3′ UTRs doing? Cold Spring Harb Perspect Biol. 2019. https://doi.org/10.1101/cshperspect.a034728
32. Warminski M, Mamot A, Depaix A, Kowalska J, Jemielity J. Chemical modifications of mRNA ends for therapeutic applications. Acc Chem Res. 2023;56(20):2814–26.
33. Whitelaw E. Globin gene transcripts can utilize histone gene 3′ end processing signals. Nucleic Acids Res. 1986;14:7059–70.
34. D.a.N MT. The translational capacity of deadenylated ovalbumin messenger RNA. Cell. 1976;8:51–8.
35. Holtkamp S, Kreiter S, Selmi A, Simon P, Koslowski M, Huber C, Türeci Oz, Sahin U. Modification of antigen-encoding RNA increases stability, translational efficacy, and T-cell stimulatory capacity of dendritic cells. Blood. 2006;108(13):4009–17.
36. Travieso T, Li J, Mahesh S, J.D.F.R.E. Mello M, Blasi. The use of viral vectors in vaccine development. Npj Vaccines 7(1) (2022).
37. Wang S, Liang B, Wang W, Li L, Feng N, Zhao Y, Wang T, Yan F, Yang S, Xia X. Viral vectored vaccines: design, development, preventive and therapeutic applications in human diseases. Signal Transduct Target Ther. 2023. https://doi.org/10.1038/s41392-023-01408-5.
38. Huang P, Deng H, Zhou Y, Chen X. The roles of polymers in mRNA delivery. Matter. 2022;5(6):1670–99.
39. Cheng Q, Wei T, Jia Y, Farbiak L, Zhou K, Zhang S, Wei Y, Zhu H, Siegwart DJ. Dendrimer-based lipid nanoparticles deliver therapeutic FAH mRNA to normalize liver function and extend survival in a mouse model of hepatorenal tyrosinemia type I. Adv Mater. 2018. https://doi.org/10.1002/adma.201805308.

40. Ye JCaZ. Lipid nanoparticle-mediated lymph node–targeting delivery of mRNA cancer vaccine elicits robust CD8 + T cell response, Proceedings of the National Academy of Sciences 119 (2022).
41. Sun D, Lu Z-R. Structure and function of cationic and ionizable lipids for nucleic acid delivery. Pharm Res. 2023;40(1):27–46.
42. Benteyn D, Heirman C, Bonehill A, Thielemans K, Breckpot K. mRNA-based dendritic cell vaccines. Expert Rev Vaccines. 2014;14(2):161–76.
43. Ma J, Ayres CM, Brambley CA, Chandran SS, Rosales TJ, Perera WWJG, Eldaly B, Murray WT, Corcelli SA, Kovrigin EL, Klebanoff CA, Baker BM. Dynamic allostery in the peptide/MHC complex enables TCR neoantigen selectivity. Nat Commun. 2025. https://doi.org/10.1038/s41467-025-56004-8.
44. Moulahoum H, Ghorbanizamani F, Zihnioglu F, Timur S. Surface biomodification of liposomes and polymersomes for efficient targeted drug delivery. Bioconjug Chem. 2021;32(8):1491–502.
45. Suzuki Y, Yakuwa M, Sato M, Samaridou E, Beck-Broichsitter M, Maeki M, Tokeshi M, Yamada Y, Harashima H, Sato Y. Splenic B cell-targeting lipid nanoparticles for safe and effective mRNA vaccine delivery. J Controlled Release. 2025. https://doi.org/10.1016/j.jconrel.2025.113687.
46. Cheng Q, Wei T, Farbiak L, Johnson LT, Dilliard SA, Siegwart DJ. Selective organ targeting (SORT) nanoparticles for tissue-specific mRNA delivery and CRISPR–Cas gene editing. Nat Nanotechnol. 2020;15(4):313–20.
47. Xu S, Liang D, Wang Q, Cheng Y, Xie D, Gui Y, Zhang H, Feng C, Zhao F, Ren W, Sun G, Yang Y, Li L, Lai Y, Fu B, Lu Y, Wang ZJ, Wu Y. In vivo genome editing of human hematopoietic stem cells for treatment of blood disorders by mRNA delivery, (2024).
48. Jiang Y, Chen S, Hsiao S, Zhang H, Xie D, Wang ZJ, Ren W, Liu M, Liao J, Wu Y. Efficient and safe in vivo treatment of primary hyperoxaluria type 1 via LNP-CRISPR-Cas9-mediated glycolate oxidase disruption. Mol Ther. 2025;33(1):104–18.
49. Kreiter S, Vormehr M, van de Roemer N, Diken M, Löwer M, Diekmann J, Boegel S, Schrörs B, Vascotto F, Castle JC, Tadmor AD, Schoenberger SP, Huber C, Türeci Ö, Sahin U. Mutant MHC class II epitopes drive therapeutic immune responses to cancer. Nature. 2015;520(7549):692–6.
50. Chen H, Li Z, Qiu L, Dong X, Chen G, Shi Y, Cai L, Liu W, Ye H, Zhou Y, Ouyang J, Cai Z, Liu X. Personalized neoantigen vaccine combined with PD-1 blockade increases CD8 + tissue-resident memory T-cell infiltration in preclinical hepatocellular carcinoma models. J Immunother Cancer. 2022. https://doi.org/10.1136/jitc-2021-004389.
51. Sahin U, Derhovanessian E, Miller M, Kloke B-P, Simon P, Löwer M, Bukur V, Tadmor AD, Luxemburger U, Schrörs B, Omokoko T, Vormehr M, Albrecht C, Paruzynski A, Kuhn AN, Buck J, Heesch S, Schreeb KH, Müller F, Ortseifer I, Vogler I, Godehardt E, Attig S, Rae R, Breitkreuz A, Tolliver C, Suchan M, Martic G, Hohberger A, Sorn P, Diekmann J, Ciesla J, Waksmann O, Brück A-K, Witt M, Zillgen M, Rothermel A, Kasemann B, Langer D, Bolte S, Diken M, Kreiter S, Nemecek R, Gebhardt C, Grabbe S, Höller C, Utikal J, Huber C, Loquai C, Türeci Ö. Personalized RNA mutanome vaccines mobilize poly-specific therapeutic immunity against cancer. Nature. 2017;547(7662):222–6.
52. Rojas LA, Sethna Z, Soares KC, Olcese C, Pang N, Patterson E, Lihm J, Ceglia N, Guasp P, Chu A, Yu R, Chandra AK, Waters T, Ruan J, Amisaki M, Zebboudj A, Odgerel Z, Payne G, Derhovanessian E, Müller F, Rhee I, Yadav M, Dobrin A, Sadelain M, Łuksza M, Cohen N, Tang L, Basturk O, Gönen M, Katz S, Do RK, Epstein AS, Momtaz P, Park W, Sugarman R, Varghese AM, Won E, Desai A, Wei AC, D'Angelica MI, Kingham TP, Mellman I, Merghoub T, Wolchok JD, Sahin U, Türeci Ö, Greenbaum BD, Jarnagin WR, Drebin J, O'Reilly EM, Balachandran VP. Personalized RNA neoantigen vaccines stimulate T cells in pancreatic cancer. Nature. 2023;618(7963):144–50.
53. Sethna Z, Guasp P, Reiche C, Milighetti M, Ceglia N, Patterson E, Lihm J, Payne G, Lyudovyk O, Rojas LA, Pang N, Ohmoto A, Amisaki M, Zebboudj A, Odgerel Z, Bruno EM, Zhang SL, Cheng C, Elhanati Y, Derhovanessian E, Manning L, Müller F, Rhee I, Yadav M, Merghoub T, Wolchok JD, Basturk O, Gönen M, Epstein AS, Momtaz P, Park W, Sugarman R, Varghese AM, Won E, Desai A, Wei AC, D'Angelica MI, Kingham TP, Soares KC, Jarnagin WR, Drebin J, O'Reilly EM, Mellman I, Sahin U, Türeci Ö, Greenbaum BD, Balachandran VP. RNA neoantigen vaccines prime long-lived CD8 + T cells in pancreatic cancer. Nature (2025).
54. Wu Y, Zeng J, Roscoe BP, Liu P, Yao Q, Lazzarotto CR, Clement K, Cole MA, Luk K, Baricordi C, Shen AH, Ren C, Esrick EB, Manis JP, Dorfman DM, Williams DA, Biffi A, Brugnara C, Biasco L, Brendel C, Pinello L, Tsai SQ, Wolfe SA, Bauer DE. Highly efficient therapeutic gene editing of human hematopoietic stem cells. Nat Med. 2019;25(5):776–83.
55. Pizzolato P. Histochemical recognition of calcium. J Histochem Cytochem. 1964;12:333–6.

Publisher's note